ELSEVIER

Physics Reports 290 (1997) 125–147

PHYSICS REPORTS

Chaotic tracer scattering and fractal basin boundaries in a blinking vortex-sink system[1]

G. Károlyi[a], T. Tél[b]

[a] *Research Group for Computational Mechanics of the Hungarian Academy of Sciences, Műegyetem rkp. 3, H-1521 Budapest, Hungary*

[b] *Institute for Theoretical Physics, Eötvös University, Puskin u. 5-7, H-1088 Budapest, Hungary*

Abstract

We consider passive tracer advection in a model of a large planar basin of fluid with two sinks opened alternately. In spite of the incompressibility of the fluid, the phase space of the tracer dynamics contains (simple) attractors, the sinks. We show that the advection is chaotic due to the appearance of a locally Hamiltonian chaotic saddle. Properties of this saddle and its invariant manifolds are investigated, and fractal and dynamical characteristics of the tracer patterns are extracted by means of the thermodynamical formalism applied to the time-delay function.

PACS: 05.45.+b; 47.32.−y

1. Introduction

The passive advection of tracer particles in hydrodynamical flows is one of the most appealing applications of the chaos theory. Assuming that inertial effects are negligible, the equation of motion for a tracer expresses the coincidence of the tracer's velocity $\dot{\boldsymbol{r}}$ with the velocity field $\boldsymbol{v}(\boldsymbol{r},t)$ of the flow that is assumed to be known: $\dot{\boldsymbol{r}}(t)=\boldsymbol{v}(\boldsymbol{r}(t),t)$. This is a simple set of ordinary differential equations for the unknown tracer motion $\boldsymbol{r}(t)$ with a given, typically nonlinear right-hand side. The solution of such an equation can be chaotic.

Advection in two-dimensional *incompressible* flows represents an important subclass of the phenomenon. The incompressibility of the flow leads then to an area conserving tracer dynamics in the phase space that coincides with the configuration space. The case of steady flows corresponds to a set of two autonomous equations of first order and, consequently, to integrable dynamics. The advection in nonsteady flows is, however, described by a driven Hamiltonian dynamics with one and a half degree of freedom. The particle motion is then typically chaotic even in the case of the simplest time-dependence of *strict periodicity*. In the last decade, a comprehensive knowledge has

[1] This paper is dedicated to Professor I. Abonyi on the occassion of his 65th birthday.

PII S0370-1573(97)00063-X

accumulated in this field both for flows in *closed* containers [1–14] and for *open* flows with asymptotic simplicity [15–33]. The tracer dynamics takes place then in a bounded or in an unbounded phase space, respectively. In the latter case, the asymptotic dynamics is simple and the tracer motion can be considered as a scattering process with all the characteristics of *chaotic scattering* [34]. In this paper we examine how the presence of *sinks or sources* influences the tracer dynamics that is then asymptotically simple but *no longer Hamiltonian*. As a consequence, global time reversal invariance does not hold, and the tracer dynamics is qualitatively different in the direct and in the time reversed dynamics.

Piecewise steady flows have long been playing an important role in understanding chaotic advection. They are maintained by keeping the flow steady for a time interval (often half of the full period), and then jumping suddenly to another flow kept steady for another time interval. Then a jump follows back to the original flow, and the whole process is repeated periodically. The corresponding particle motion is then a kind of kicked dynamics due to the sudden jumps in the flow field. A pioneering example of this kind is Aref's blinking vortex system [1]. Another famous model for stirring in closed regions is related to the journal bearing flow [2, 3] whose experimental realisation was also possible [3, 4]. A piecewise steady model for open flows with Hamiltonian particle dynamics, introduced recently, is based on a periodic repetition of a vortex action and of a homogenous flow [27].

In order to study the effect of asymptotic dissipation in the particle dynamics of a piecewise steady model, we shall investigate the blinking vortex-sink system of Aref et al. [17]. It models the *outflow* from a large bath tub with two sinks that are opened in an alternating manner. In the course of this process, a chaotic mixing might take place. Note that the time reversed model describes the periodic *injection* of fluid into the basin via two different sources accompanied with rotation, and can be called a blinking vortex-source system. It represents a model of mixing due to injection. We show that, despite of the qualitatively different forward and backward global dynamics, both systems have a common *nonattracting set* with Hamiltonian local dynamics. This invariant set is responsible for the mixing in both the direct and the time reversed tracer motion.

The problem of *fractal dye boundaries* in open flows has recently been addressed [17, 28–33] in the context of Hamiltonian dynamics. The blinking vortex-sink system is ideally suited for studying basin boundaries because it has two attractors (the two sinks) and a well-defined basin of attraction. The original aim of Aref et al. in [17] was to show that this boundary can turn to be a fractal in a broad range of parameters. We shall explain their finding in terms of the nonattracting set: the basin boundary is the stable manifold of this set and becomes a *fractal* as soon as the set becomes *chaotic*. Thus, the fractality of the boundary is a unique sign of chaotic advection, and vice versa.

The paper is organized as follows. In Section 2 the advection in the velocity field of the blinking vortex-sink system is described, and the tracer dynamics is represented by a stroboscopic mapping. Then in Section 3 we explain the transient chaotic behaviour of the advected particles by means of an invariant chaotic saddle governing the discrete dynamics. In Section 4 this explanation is extended by examining the time evolution of the chaotic saddle and its invariant manifolds. Due to the explicit form of the tracer map, we are able to study the dependence of the dynamics in a large range of the vortex and sink strengths (Section 5). Multifractal and dynamical properties of the saddle are determined by means of the thermodynamical formalism in Section 6. Finally, in Section 7 concluding remarks are given along with a discussion of multicolored dye boundaries.

2. The blinking vortex-sink model and the advection map

An ideal fluid filling in the infinite plane with a point vortex in it that is simultaneously sinking can be a model of a shallow but infinite basin of fluid with a sink. This corresponds to the observation that a rotational flow is formed around the sink in the course of drainage.

The velocity field due to the sink is thus modelled by the superposition of the potential flows of a point sink and of a point vortex. The complex potential [35] for a sinking vortex point located at the origin can be written as

$$w(z) = -(C + \mathrm{i}K)\ln z\,, \tag{1}$$

where z is the complex coordinate in the plane of the flow. Here $2\pi C$ is the sink strength, i.e. the amount of fluid drained by the sink in unit time, and $2\pi K$ is the circulation measuring the vortex strength. The velocity field corresponding to $w(z)$ consists of the superposition of a radial component $v_r = -C/r$ and of a tangential component $v_\varphi = K/r$. The imaginary part of the complex potential, $\Psi = -K\ln r - C\varphi$ is the streamfunction [35]. The streamlines (the level lines of Ψ) are logarithmic spirals: $\varphi = -K/C\ln r +$ const.

A passively advected tracer particle follows the velocity field of the flow without any inertia. Its equations of motion in polar coordinates are

$$\dot{r} = v_r\,, \qquad \dot{\varphi} = v_\varphi/r\,. \tag{2}$$

By solving these equations with initial conditions (r_0, φ_0), we find

$$\begin{aligned} r(t) &= (r_0^2 - 2Ct)^{1/2}\,, \\ \varphi(t) &= \varphi_0 - (K/C)\ln r(t)/r_0\,. \end{aligned} \tag{3}$$

The particles move along streamlines as the flow is stationary. By returning to the complex representation, $z = r\exp(\mathrm{i}\varphi)$, we obtain that a tracer particle starting at a point z_0 will arrive, after time t, at

$$z(t) = z_0(1 - 2Ct/|z_0|^2)^{1/2 - \mathrm{i}K/2C}\,. \tag{4}$$

Because the motion is undefined after reaching the sink center, the time in this expression has to be limited from above:

$$t \le |z_0|^2/(2C)\,. \tag{5}$$

With this condition, Eq. (4) uniquely describes the tracer motion.

The *blinking vortex-sink system* [17] is obtained by having two such sinking vortex points some distance apart from each other, both being active alternately for a duration of $T/2$. In this system the velocity field is periodic with T, but in a special way: it is stationary for half a period and stationary again but of another type for the next half period $T/2$. The velocity field corresponds to a sinking vortex flow centered at $z = -a$ and at $z = a$ in the time intervals $(0, T/2]$ and $(T/2, T]$, respectively. The entire flow is no longer stationary, there are jumps in the velocity field at each half period.

The tracer motion can be easily built up from Eq. (4). A trajectory starting at $t = 0$ follows the corresponding streamline up to $t = T/2$, when the velocity field suddenly changes. Then, the tracer finds itself on another streamline that will be followed for the next time interval of length $T/2$. Thus,

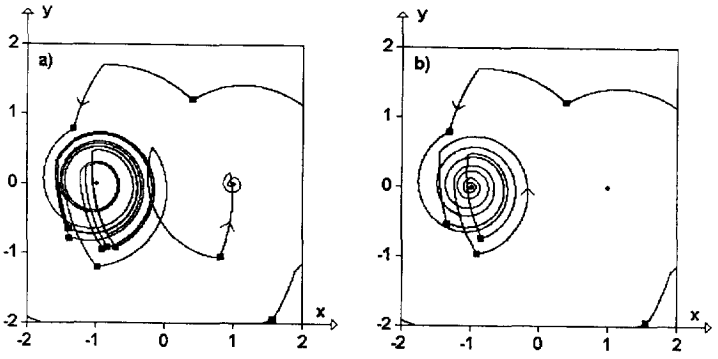

Fig. 1. Two different tracer trajectories in the vortex-sink system for the parameter values $\eta = 0.5$, $\xi = 10$ with initial conditions differing by an amount of 10^{-2}. Breakpoints are due to the sudden jumps in the velocity field of the flow. Black dots denote the vortex-sink centers. Black squares at the breakpoints mark the discrete time trajectories for the $t_0 = 0$ stroboscopic map. The tracers of cases (a) and (b) leave the flow through different sinks, providing an example for the sensitive dependence on initial conditions.

on a time scale of several periods, the trajectory will have several break points and can be much more complicated than any of the streamlines. Fig. 1 presents such trajectories.

Since the velocity field is periodic, it is convenient to monitor the particle motion on a *stroboscopic map* obtained by recording the position of particles after integer multiples of T only. In this section we choose the starting time of taking stroboscopic snapshots t_0 to be $t_0 = 0$ corresponding to the instant when the right sink is switched off. For the tracer position at $t = T/2$ and $t = T$ we obtain from Eq. (4) by a simple coordinate transformation that they are

$$z(T/2) = (z_0 + a)\left(1 - \frac{CT}{|z_0 + a|^2}\right)^{1/2 - iK/2C} - a\,,$$

and

$$z(T) = (z(T/2) - a)\left(1 - \frac{CT}{|z(T/2) - a|^2}\right)^{1/2 - iK/2C} + a\,, \tag{6}$$

respectively. By introducing dimensionless coordinates via $z \to az$, one notices that the dynamics is fully specified by two parameters:

$$\eta = CT/a^2 \quad \text{and} \quad \xi = K/C\,, \tag{7}$$

the dimensionless sink strength and the ratio of the vortex to sink strength, respectively. The locations of the sinking vortex points are $z = \pm 1$ in the new, dimensionless units.

The rule connecting the coordinates on snapshots taken at $t = 0$ and $t = T$ is exactly the same as for the $t = nT$ and $t = (n+1)T$ stroboscopic instants. By introducing $z_n \equiv z(nT)$ as the particle position after n periods, we obtain the general form of the discrete time advection dynamics as

$$z_{n+1} = (z_n' - 1)\left(1 - \frac{\eta}{|z_n' - 1|^2}\right)^{1/2 - i\xi/2} + 1\,,$$

where

$$z'_n = (z_n + 1)\left(1 - \frac{\eta}{|z_n + 1|^2}\right)^{1/2 - i\xi/2} - 1 \tag{8}$$

is a dummy variable corresponding to the particle position at $t = (n + 1/2)T$. It is the jump in the flow field at $t = T/2 \bmod(T)$ that made the submaps connecting z_n to z'_n, and z'_n to z_{n+1} different.

We note that due to the alternating character of the flow, *effective sink cores* have been formed. Tracers which are inside a circle of radius $R = \sqrt{\eta}$ around any of the sinks at the instant when it starts to be active, will leave the system in the next time interval of $T/2$. We do not follow their dynamics but take into account that particles having entered these disks disappear from the map. This formally corresponds to having infinitely strong dissipation within the sink cores. Thus, the sink cores are extended nonchaotic *attractors* of the advection map (although the time continuous tracer dynamics possesses point attractors only, the two centers). Therefore, Eqs. (8) are valid outside of these sink cores only. Here, however, the map has Hamiltonian character: it is area-preserving and invertible.

It is worth mentioning a simple symmetry property. The map is invariant under the transformation $t \to t + T/2$ and $z \to -z$, i.e. under the time shift of a half period and the reflection with respect to the origin. This is due to the fact that the flow is invariant under the transformation of exchanging the vortex-sink centers and shifting the time by half a period.

For $\xi = 0$ we obtain a pulsed sink system without any rotation similar to the pulsed source-sink system introduced by Jones and Aref [16], but numerical evidence shows that the tracer dynamics is regular for any value of η. In the limit $\eta \to 0$, $\xi \to \infty$, so that $\eta\xi = \text{const}$, we recover the blinking vortex system of Aref [1] that exhibits chaotic advection in a closed region. In what follows, we shall deal with the properties of the advection map Eq. (8), and its parameter dependence in the finite η and ξ regime.

3. The chaotic saddle and its invariant manifolds

For a detailed investigation we choose the parameter values $\eta = 0.5$ and $\xi = 10$. Two complicated tracer trajectories have already been shown in Fig. 1. Although there is only a slight difference in the initial conditions, the shapes of the trajectories are rather different, and the tracers finally leave the system through different sinks.

It is instructive to look for periodic orbits since if they exist, they certainly are examples for orbits never leaving the system, i.e., never reaching the attractors. At these parameter values we found three period–one orbits whose forms (both continuous time and discrete representations) are shown in Fig. 2. They turn out to be all hyperbolic with local Lyapunov exponents on the order of 2.

The key observation for understanding the complicated dynamics is the existence of a strange *invariant chaotic set*, a chaotic *saddle* in the system. The saddle is *nonattracting*, and lies in the Hamiltonian part of the space, outside of the attractors. The saddle consists of all the countable infinite number of unstable periodic orbits of the mapping. It also contains an uncountable infinite number of non-periodic orbits [37], the ones never reaching any of the sinks in the direct dynamics, and being bounded to a finite region in the time reversed dynamics. The tracers leaving the system

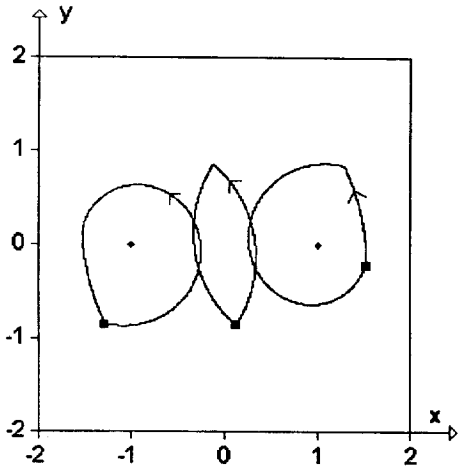

Fig. 2. Three period-one orbits for the parameter values $\eta = 0.5$, $\xi = 10$. Black dots denote the vortex-sink centers. Black squares mark the discrete time orbits, the three fixed points of the $t_0 = 0$ stroboscopic map. The Lyapunov exponent of the symmetric and the two asymmetric orbits is 2.03 and 1.97, respectively.

after only a long time are those coming close to the chaotic saddle. The stroboscopic picture of this invariant set is shown in Fig. 3(a). All the points of the saddle seem to be hyperbolic, having different stable and unstable directions.

The entire saddle has a *stable manifold*. This set is formed by points that can come arbitrarily close to the saddle in the future (of the direct dynamics). The *unstable manifold* of the saddle is the set along which the particles having reached the saddle with high accuracy leave it after a long time. More precisely, the unstable manifold is the stable manifold of the time reversed tracer dynamics. These invariant manifolds are shown in Figs. 3(b) and (c). The invariant set is the common part of the stable and unstable manifolds. Since both the stable and the unstable manifolds are lines with Cantor-set-structure in their intersections, the chaotic saddle also has Cantor-set-structure both in its stable and unstable directions. Thus, the invariant set appears as a (slightly distorted) direct product of two Cantor sets.

In chaotic systems, it is worth considering ensembles of particles instead of isolated ones because the ensembles have well-defined averages. In a hydrodynamical problem the ensemble has a clear physical interpretation as a droplet of tracers. Let us therefore briefly investigate the droplet dynamics. If a droplet overlaps with the stable manifold, it moves in the direct dynamics towards the saddle. Particles starting *exactly* from the stable manifold will hit the chaotic saddle, and thus they will never leave the system. Particles starting near enough to the stable manifold are advected in the vicinity of the chaotic saddle and stay there for a long time. Finally these long living tracers will leave the system along the unstable manifold (see Fig. 4). Consequently, the shape of the droplet after sufficiently long time traces out with a high accuracy the unstable manifold. This invariant set becomes thus a direct observable in the droplet dynamics. In fact, the unstable manifold of Fig. 3(b) was numerically obtained as the shape of a droplet of size 0.5×0.5 after $n = 4$ steps.

In the time reversed system the role of the stable and unstable manifolds is interchanged. Since the time reversed system can be interpreted as a blinking vortex-source model, the stable (unstable)

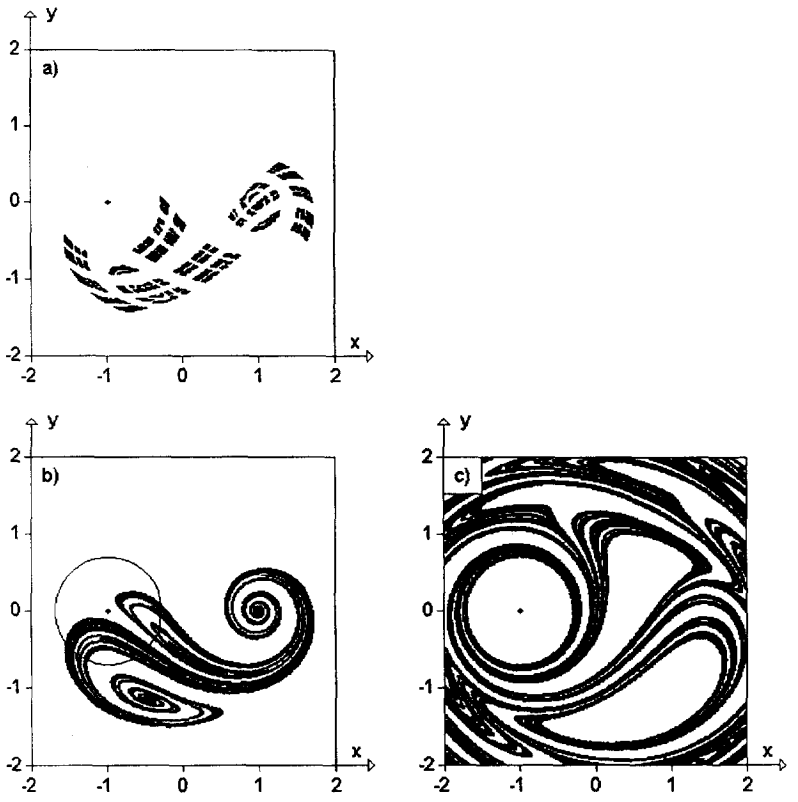

Fig. 3. Invariant sets of the tracer dynamics in the vortex-sink system on the $t_0 = 0$ stroboscopic map, Eq. (8), for $\eta = 0.5$, $\xi = 10$. (a) The chaotic saddle is the set of orbits never reaching the attractors either in the direct or in the time reversed dynamics. It is the direct product of two Cantor sets. (b) The saddle's unstable manifold is the set of initial conditions leading to the saddle in the time reversed dynamics. The circle around the $(-1,0)$ sink encloses the attractor on the left half-plane, i.e., the area leaving the system in the next half-period. (c) The saddle's stable manifold is the set of initial conditions leading to the saddle. It coincides with the basin boundary of the two attractors.

manifold of the original system corresponds to the unstable (stable) manifold of the latter, while the chaotic saddle is the same for both systems. A droplet originally overlapping with the stable manifold of the time reversed dynamics will thus trace out the unstable manifold, i.e. the stable manifold of the vortex-sink system (Fig. 5). The stable manifold of Fig. 3(c) was numerically determined as the $n = 6$th image of a droplet of size 0.5×0.5 in the time reversed dynamics. The chaotic sets shown in the paper (as e.g. Fig. 3(a)) were obtained as common parts of stable and unstable manifolds.

Finally, we connect the concept of invariant manifolds to that of the basin boundaries whose study was the original motivation of the authors of Ref. [17]. A natural definition of a basin in the vortex-sink problem is the set of all points leaving the system via a given sink. The boundary between the basins of the left and right sinks has to contain, therefore, points never leaving through any of the sinks. Boundary points must thus tend to the chaotic saddle. Consequently, the *basin boundary is the saddle's stable manifold.* A comparison of Fig. 3(c) with the basin boundary generated in

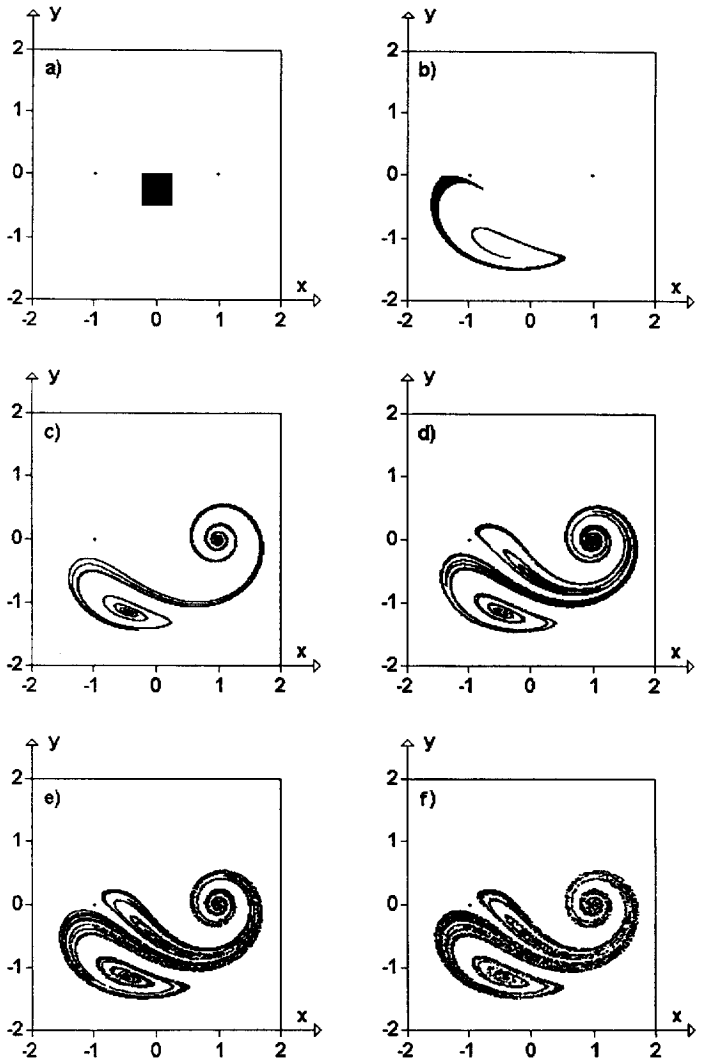

Fig. 4. Time evolution of a droplet of 300×300 particles uniformly distributed over the region $[-0.25, 0.25] \times [-0.5, 0]$ on the $t_0 = 0$ stroboscopic map, Eq. (8) (parameter values $\eta = 0.5$, $\xi = 10$). The pictures show the shape of the droplet at discrete times 0, 1, 2, 3, 4 and 5 (a,...,f). After already $n = 4$ steps the droplet traces out the unstable manifold with an accuracy of resolution better than 1 percent.

Ref. [17] for the same parameter setting supports this statement. In the vortex-source system, a basin can be defined as the set of all points injected into the flow via a given source. Consequently, the basin boundary is the saddle's stable manifold in this system, i.e., the saddle's unstable manifold in the vortex-sink system. In any case, the fractality of the basin boundary is a unique sign of the chaoticity of the tracer dynamics. We shall see later (in Section 5) that for certain parameter values the chaotic saddle does not exist, the nonattracting set is a single periodic orbit with smooth manifolds. The basin boundary is then indeed a nonfractal curve.

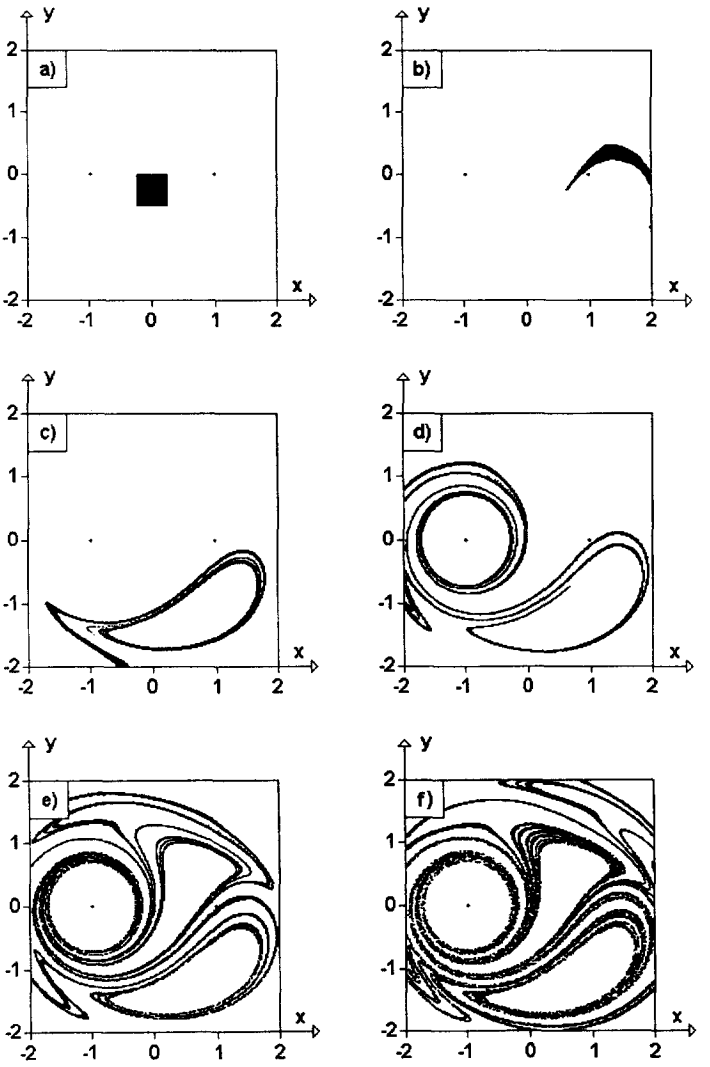

Fig. 5. Time evolution of a droplet of 300×300 particles uniformly distributed over the region $[-0.25, 0.25] \times [-0.5, 0]$ on the time reversed $t_0 = 0$ stroboscopic map (parameter values $\eta = 0.5$, $\xi = 10$). The pictures show the shape of the droplet at discrete times 0, 1, 2, 3, 4 and 5 (a,...,f). The convergence towards the stable manifold is slower due to its large extension but even so inside a circle of radius 1.5 the deviation between the droplet and the manifold is less than 1% after 5 steps already.

4. Time dependence of the invariant sets

The stroboscopic snapshots can be taken not only at $t_0 = 0 \bmod(T)$. One can choose arbitrary starting times t_0, and record the tracers' positions at the time instants $t = nT + t_0$ as $z_n(t_0)$. Varying t_0 between 0 and T we get different discrete-time representations of the tracer dynamics. A series of pictures showing the invariant sets on the stroboscopic map taken at different times t_0 can be

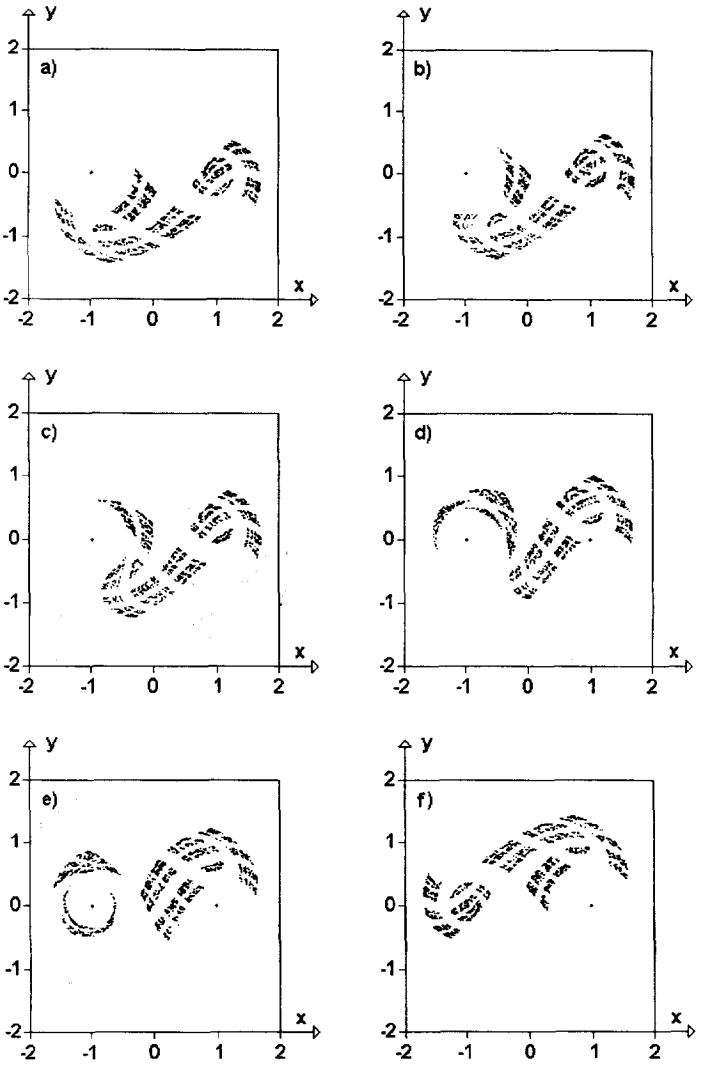

Fig. 6. The chaotic saddle's temporal evolution for the parameter values $\eta = 0.5$, $\xi = 10$. The pictures show the chaotic saddle at times $\tau = 0$, $\frac{1}{16}$, $\frac{2}{16}$, $\frac{4}{16}$, $\frac{6}{16}$ and $\frac{8}{16}$ mod(1) (a,...,f). The saddle for $\tau \geq \frac{1}{2}$ is the mirror image of the one at $\tau - \frac{1}{2}$ taken with respect to the origin.

considered as the (periodic) time evolution of these sets. Without loss of generality, we can assume that $t_0 < T/2$ because the symmetry properties of the system guarantee that the behaviour after a time shift of $T/2$ is the same if a reflection is applied with respect to the origin.

Using the results of the previous sections, we can easily determine the position of a tracer after a time-period T, if it starts from z_n at time $nT + t_0$. First, we determine its position at $(n + 1/2)T$ from Eq. (4) as

$$z'_{n,\tau} = (z_{n,\tau} + 1)\left(1 - \frac{\eta(1 - 2\tau)}{|z_{n,\tau} + 1|^2}\right)^{1/2 - i\xi/2} - 1\,, \tag{9}$$

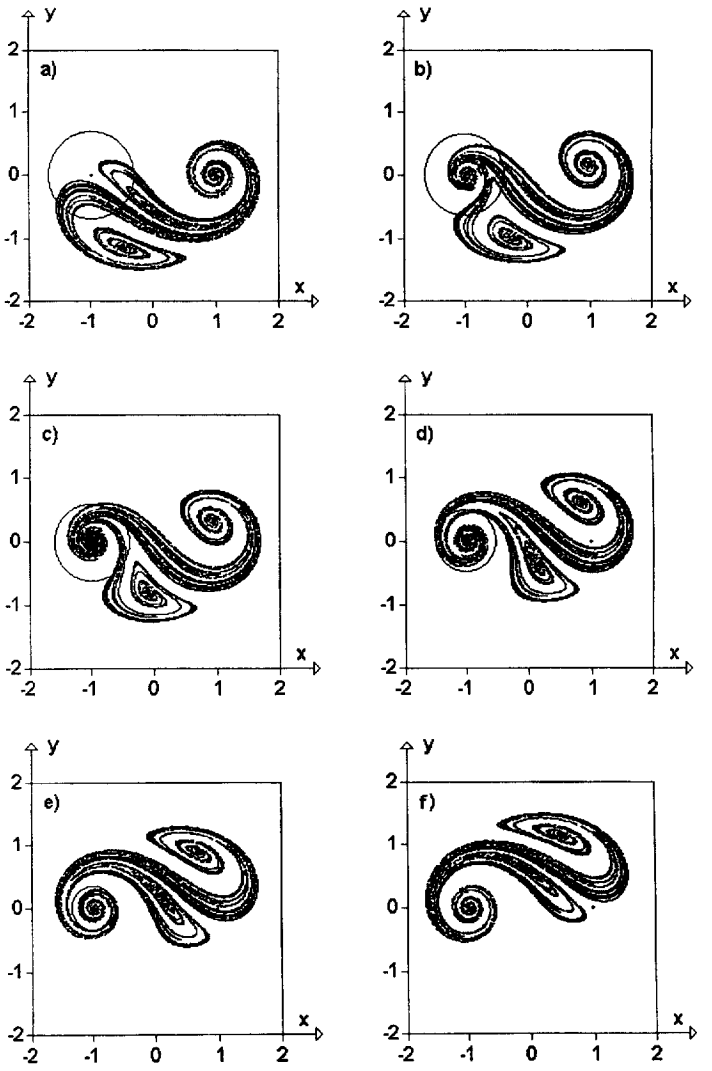

Fig. 7. Temporal evolution of the saddle's unstable manifold in the vortex-sink system for the parameter values $\eta = 0.5$, $\xi = 10$. The time instants corresponding to the pictures are the same as in Fig. 6. The manifold for $\tau \geq \frac{1}{2}$ is the mirror image of the one at $\tau - \frac{1}{2}$ taken with respect to the origin. The manifold was obtained with the droplet method after $n = 4$ iterations. Note that the most drastical changes occur in the first interval of length one sixteenth because there are points very close to the newly opened sink at $(-1, 0)$, and the angular velocity of the rotation increases as r^{-2} where r is the distance from the sink. The effective sink cores (attractors) are shown as circles around $(-1, 0)$.

because the particle is advected by the sinking vortex at $z = -1$ for a duration of $T/2 - t_0$ only. Here we have introduced the dimensionless time (or phase) parameter $\tau \equiv t_0/T$. The position of this tracer at $t = (n+1)T$ is obtained according to the first line of Eq. (8) as

$$z''_{n,\tau} = (z'_{n,\tau} - 1)\left(1 - \frac{\eta}{|z'_{n,\tau} - 1|^2}\right)^{1/2 - i\xi/2} + 1 . \tag{10}$$

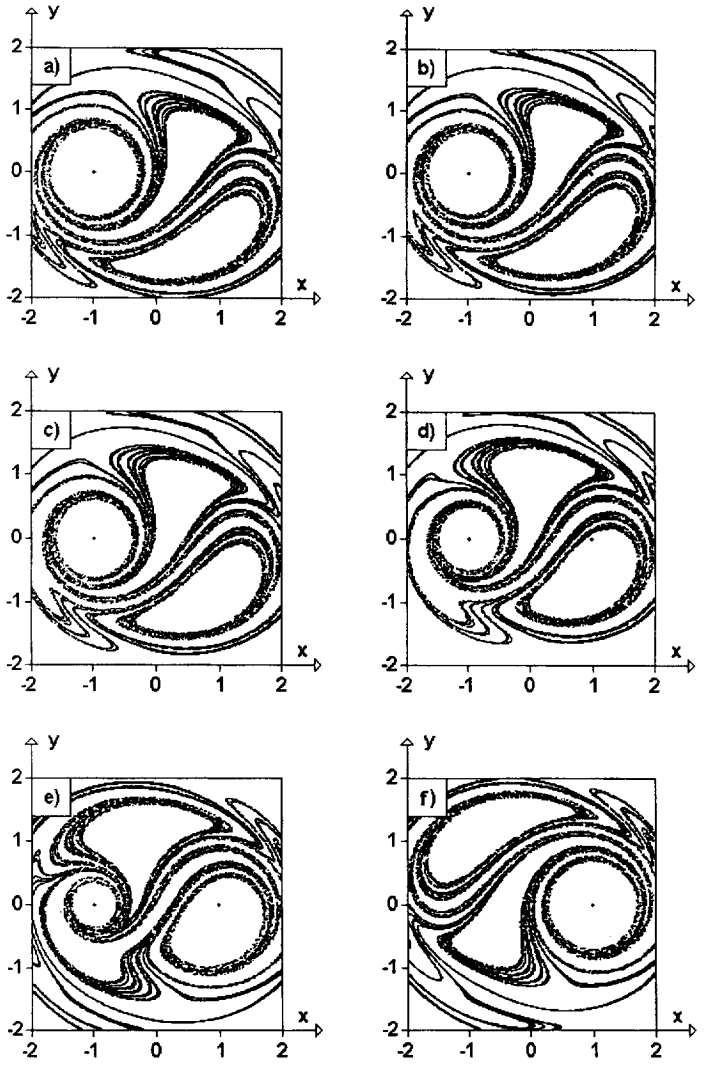

Fig. 8. Temporal evolution of the saddle's stable manifold in the vortex-sink system for the parameter values $\eta = 0.5$, $\xi = 10$. The time instants corresponding to the pictures are the same as in Fig. 6. The manifold for $\tau \geq \frac{1}{2}$ is the mirror image of the one at $\tau - \frac{1}{2}$ taken with respect to the origin. The plot was obtained by means of the time reversed droplet method after $n = 6$ iterations. Reading the pictures in reversed order (f,e,...,a), the evolution of the black line corresponds to the evolution of the boundary separating particles injected into the flow via different sources in the blinking vortex-source system. Picture (f) corresponds to an instant when the right source stops and the left one starts injecting.

Then the tracer is advected again by the left sinking vortex for the remaining time interval of length t_0, and arrives finally at

$$z_{n+1,\tau} = (z''_{n,\tau} + 1)\left(1 - \frac{2\eta\tau}{|z''_{n,\tau} + 1|^2}\right)^{1/2 - i\xi/2} - 1 . \tag{11}$$

The time evolution of the chaotic saddle is presented in Fig. 6 for the parameter values $\eta = 0.5$, $\xi = 10$. Since this is the set of points staying in a finite region forever and never reaching any of the attractors in both the direct and in the time reversed dynamics, its behaviour has entirely Hamiltonian character. The shape of the saddle changes periodically in time. It does not mean, however, that all the points of the set return to their original position after a certain time. There are uncountably many points of the saddle with chaotic trajectories. In fact, the entire set moves as if the points of Fig. 3(a) were advected by the flow. Since the advection is a smooth transformation, the fractal dimension of the saddle is the same on all snapshots.

Similarly, we can determine the time evolution of the saddle's unstable manifold (see Fig. 7). It is special in the sense that the number of points starting on this set decreases exponentially, although the geometrical shape is moving periodically. We note that after the right sink is closed at $t_0 = 0$, there is an interval in τ when the unstable manifold of the map is not connected with any of the sinks. This fact is again due to the sudden jump in the velocity field of the flow. The evolution of the saddle's stable manifold is illustrated in Fig. 8. Just like the chaotic saddle itself, its manifolds change their shape as if they were advected by the flow.

5. Parameter dependence

Tracers with long life times typically approach the system's nonattracting set (that can be either a chaotic saddle or some unstable periodic orbits) along its stable manifold, then remain in the vicinity of this set for a transient period and follow the dynamics on it. Later they leave the set along its unstable manifold and reach one of the attractors. Therefore, the tracer behaviour in the blinking vortex-sink or vortex-source system strongly depends on how the nonattracting set changes when the two dimensionless parameters η and ξ are varied. Fig. 9 shows the nonattracting invariant sets for 16 different pairs of η and ξ on the $t_0 = 0$ stroboscopic map. From the top to the bottom η, the sink strength, decreases, while from the left to the right ξ, the ratio of the vortex to the sink strength, increases. For parameter values where the system is non-chaotic (small η or ξ values, lower left triangle region), the nonattracting set has numerically been found to consist of one point only, a hyperbolic period-one orbit. Our numerical investigations suggest that the chaotic saddle appears suddenly as the parameters are changed. Periodic orbits are born in a very tiny region around the unstable period-one orbit in a similar way as in the course of the abrupt bifurcation in chaotic scattering [36]. We can also observe in Fig. 9 that after chaos has appeared, the size of the chaotic saddle grows with ξ. For some (typically large) ξ values there are also extended areas surrounded by the chaotic saddle. Such regions are present e.g. in the upper right picture of Fig. 9 and are due to the fact that stable periodic orbits (elliptic points) have appeared surrounded by KAM tori.

Three different types of tracer behaviour thus can occur depending on the parameters, similarly as in other models [28, 30]. The first is a simple nonchaotic motion with only one point as the nonattracting invariant set. This point is hyperbolic with two real eigenvalues. The second is a chaotic behaviour with a fully hyperbolic chaotic saddle. This nonattracting invariant set has a structure of the direct product of two Cantor-sets. The third type of behaviour is also chaotic, but with an invariant set consisting both of a hyperbolic and a nonhyperbolic component. The latter component appears around the KAM tori. In this region the local Lyapunov exponents can take on

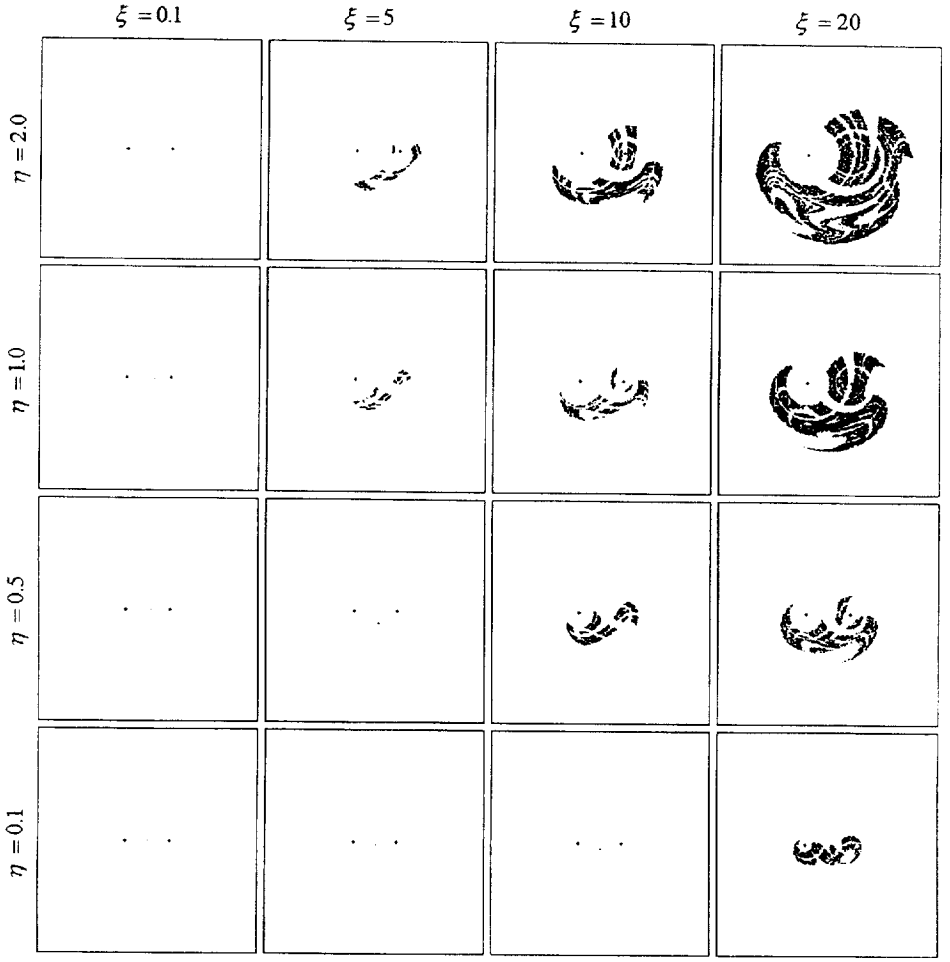

Fig. 9. The $t_0 = 0$ stroboscopic section of the nonattracting set for different parameter values. The $[-5,5] \times [-5,5]$ region of the (x, y) plane is shown; the vortex-sink centers are denoted by black dots. For small η and ξ values the nonattracting set consists of one single hyperbolic fixed point only, in other regions chaotic saddles exist.

arbitrarily small positive values. Consequently, tracers coming close to the torus will stay there for anomalously long times. (Note that tracers starting *inside* a torus cannot escape, they remain to be trapped there forever. KAM tori – if they exist – form the boundary of fluid blobs of finite area that never become drained from the system.)

The saddle's unstable manifold is qualitatively different for the parameter values corresponding to chaotic and nonchaotic cases. This is clearly visible in Fig. 10. The unstable manifold is a simple curve in the lower left pictures associated with nonchaotic behaviour corresponding to the single period-one orbit as the nonattracting set. For the parameter values where the nonattracting set is a fractal, the unstable manifold is also a complicated winding curve. As the parameter values η or ξ grow, the extension of the unstable manifold increases. The circle around the left sink shows the attractor on the advection map. Clearly, for all cases this circle contains a certain part of the

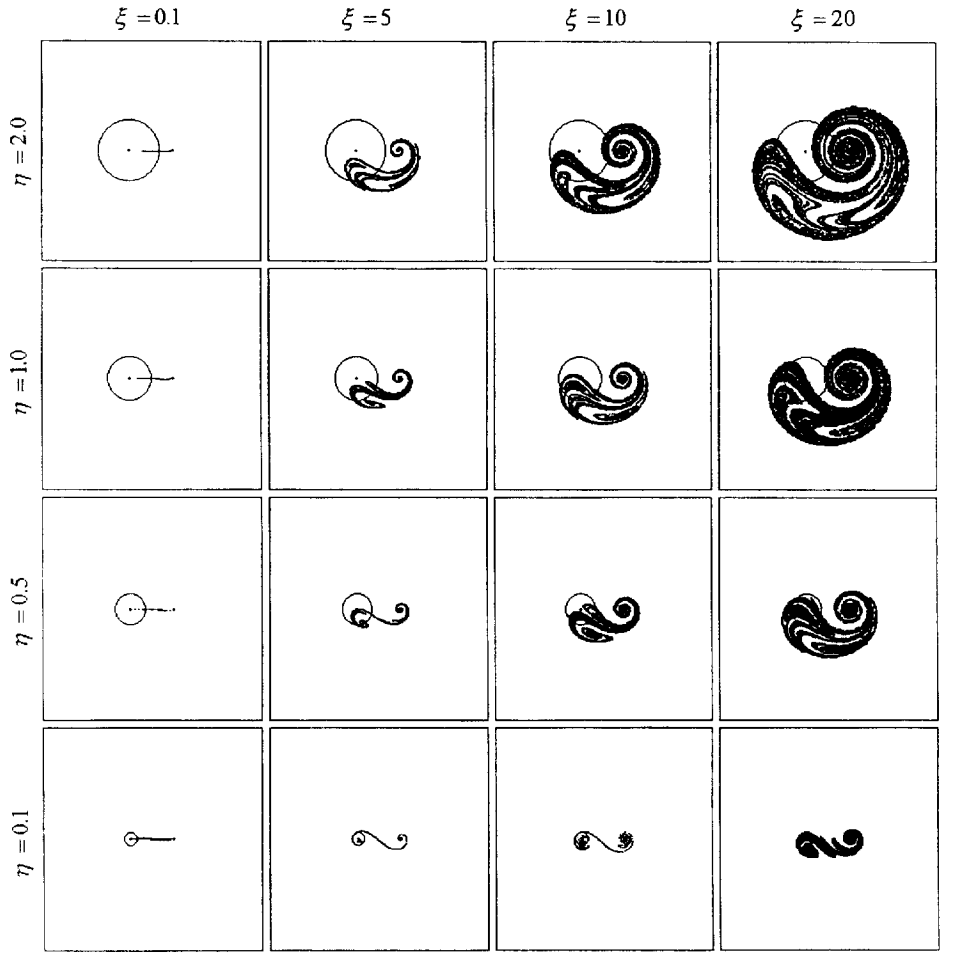

Fig. 10. The $t_0 = 0$ stroboscopic section of the nonattracting set's unstable manifold in the vortex sink–system for different parameter values in the same region as in Fig. 9. The circles around $(-1, 0)$ indicate the left attractor of the advection map. For small η and ξ the unstable manifold consists of a line segment only. In other regions it is a complicatedly winding fractal curve.

unstable manifold corresponding to the fact that the unstable manifold directs the particles into the attractor(s).

The saddle's stable manifold is shown in Fig. 11 for the 16 different parameter pairs considered. They are again simple line segments for the nonchaotic cases, where the nonattracting invariant set is a single point, and complicated fractal curves where a chaotic saddle is formed.

6. Extracting fractal and dynamical properties

Almost all the tracers leave the system after a certain time (apart from those starting from islands surrounded by KAM tori). This escaping property assures that the chaotic behaviour is restricted to

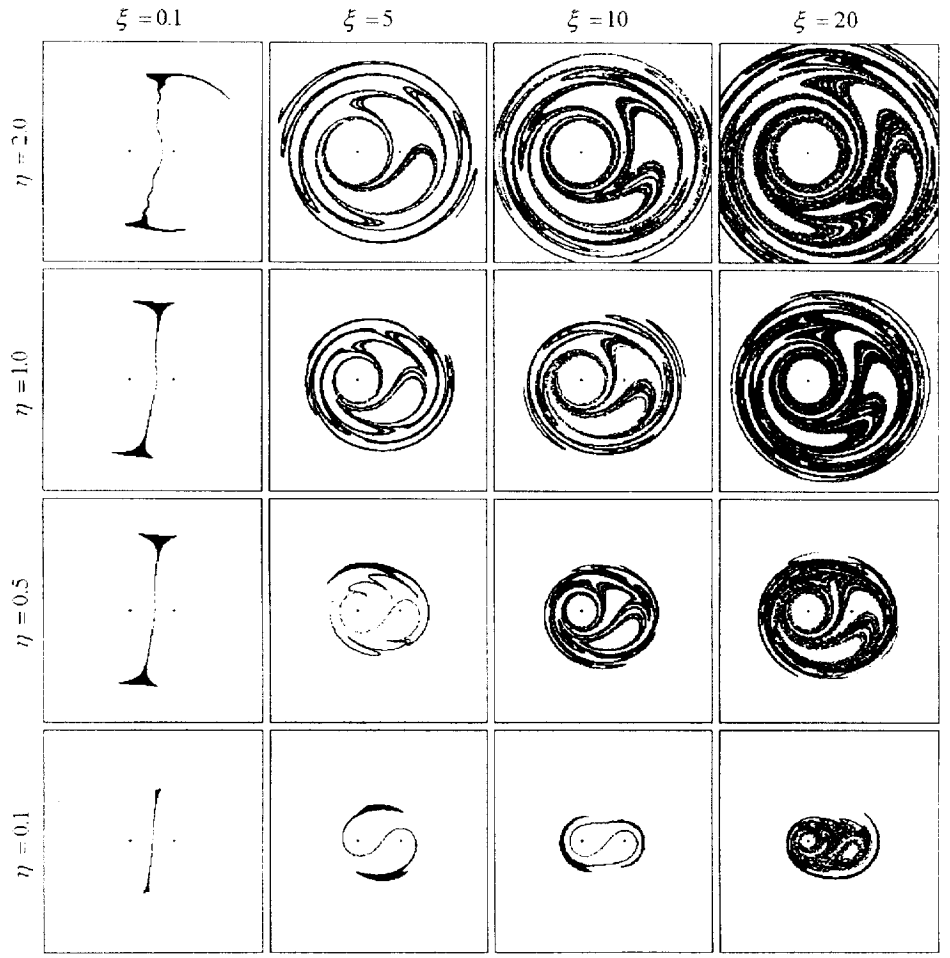

Fig. 11. The $t_0 = 0$ stroboscopic section of the stable manifold in the vortex-sink system for different parameter values in the same region as in Fig. 9. For small η and ξ the stable manifold consists of a line segment only. In other regions it is a complicatedly winding fractal curve. The large black areas are due to the finite resolution and the finite number of steps ($n = 8$) taken in the time reversed droplet method to generate the manifold.

a finite domain both in space and time. Therefore, by applying the results of the theory of transient chaos [37] and chaotic scattering [34], it is possible to define a *natural measure* on the nonattracting chaotic saddle. Calculating the average Lyapunov exponent with respect to this measure, it can be positive. Other relevant characteristics of chaos can also be determined.

A quantity of central importance is the *time-delay function*. It is defined as the number of steps the tracers need to reach any of the attractors as a function of their initial coordinate along a line segment. For the parameter values $\eta = 0.5$, $\xi = 10$ Fig. 12 shows this function for initial coordinates taken along a straight-line segment. It has a well defined, hierarchical structure with singularities on a Cantor set formed by the intersections with the saddle's stable manifold. Taking into consideration that the whole saddle is contained in the Hamiltonian region of the flow, the properties of the saddle

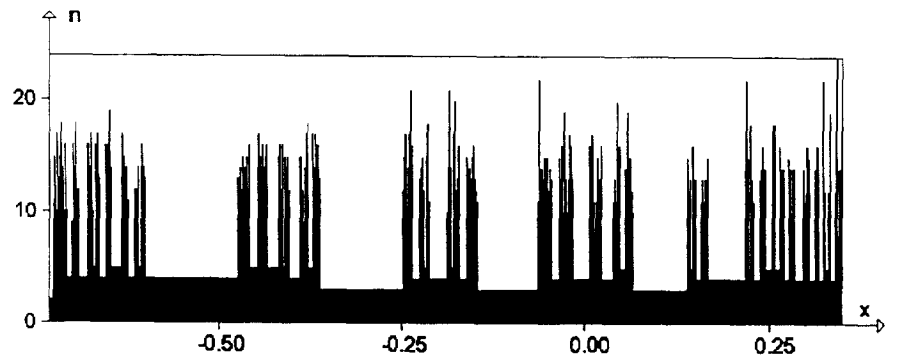

Fig. 12. A discrete time-delay function in the vortex-sink system for $\eta = 0.5$, $\xi = 10$. The picture shows the number of periods (n) the tracers, starting from the line $x \in [-0.73, 0.35]$, $y = 1$, need to leave the system through any of the sinks. The fractal structure emerges in the limit of extremely long exit times.

must be the same along both the stable and unstable directions. Thus, it is sufficient to examine the statistical features on the intersection of the stable manifold with a straight line – the time-delay function – to get relevant information about the entire chaotic saddle. The use of the thermodynamical formalism [38] is very well suited for this purpose.

The scaling behaviour of the time-delay function and of the chaotic saddle can be fully characterized by the so-called free energy function [37–39]. Let us consider the intervals of the initial conditions on the time-delay function where the delay is larger or equal to n. We denote the length of the ith such interval by $l_i^{(n)}$. By increasing n, one finds more and more intervals with shorter and shorter sizes. Taking the limit $n \to \infty$ resembles thus to performing the construction of a Cantor set. It is therefore natural to expect that fractal and other properties can be extracted from the interval hierarchy.

The free energy function $F(\beta)$ is defined by

$$\sum_{i=1}^{N(n)} (l_i^{(n)})^{\beta} \sim \mathrm{e}^{-\beta F(\beta) n}, \tag{12}$$

for $n \gg 1$, where $N(n)$ is the number of intervals on the nth level of the hierarchy, and β is any real number. The free energy characterizes the length scale distribution of the intervals covering the singularities in the time delay function. These intervals are transported away by the flow along the stable manifold, are slightly deformed, and after a certain time approach the saddle. The chaotic saddle's coverage with short intervals along its unstable manifold has thus the same scaling properties as the intervals in the time delay function. Therefore, the same free energy characterizes the chaotic saddle, too [39].

The total length of the intervals $l_i^{(n)}$ on the nth level is proportional to the number of the tracers staying in the flow after n iterations of the map. Thus, the *escape rate* κ characterizing the exponential decay of the tracers remaining in the system is calculated as $\beta F(\beta)$ taken at $\beta = 1$. The reciprocal of κ is the average lifetime of the chaotic tracer dynamics. The *topological entropy* K_0 describing the exponential growth of the number of the intervals $N(n)$ with n (as $\exp(K_0 n)$) can be deduced again from Eq. (12) taken at $\beta = 0$. Two other important dynamical properties can be derived from

Table 1
Basic chaos characteristics determined from the thermodynamical formalism for different parameter values. The table shows the values of the escape rate κ, the average Lyapunov exponent $\bar{\lambda}$, the partial fractal dimension d_0 and the topological entropy K_0 for the 16 pairs of parameter values of Fig. 9. From these quantities the information dimension and the metric entropy can easily be obtained as $d_1 = 1 - \kappa/\bar{\lambda}$, and $K_1 = \bar{\lambda} - \kappa$, respectively, [37, 38]

			ξ			
			0.1	5	10	20
		κ	2.20	0.8	0	0
	2	$\bar{\lambda}$	2.20	2.67	0	0
		d_0	0	0.59	1	1
		K_0	0	1.25	2.30	4.21
		κ	1.03	1.08	0.54	0
	1	$\bar{\lambda}$	1.03	3.46	2.19	0
		d_0	0	0.56	0.69	1
η		K_0	0	1.60	1.30	2.50
		κ	0.51	1.20	0.66	0.41
	0.5	$\bar{\lambda}$	0.51	3.00	2.44	2.16
		d_0	0	0.53	0.74	0.79
		K_0	0	1.13	2.11	1.90
		κ	0.10	0.50	0.92	0.30
	0.1	$\bar{\lambda}$	0.10	0.50	0.92	2.00
		d_0	0	0	0	0.83
		K_0	0	0	0	1.86

the free energy function: the average Lyapunov exponent $\bar{\lambda}$ on the nonattracting set is the derivative of $\beta F(\beta)$ at $\beta = 1$, while the fractal dimension d_0 of the singularities in the time-delay function is the value of β where F vanishes. Since the singularities are projections of the nonattracting set on a curve roughly parallel to the unstable manifold, d_0 is also called the partial fractal dimension of the saddle. These most important characteristics can thus be extracted from the free energy as [1]

$$\kappa = F(1), \qquad K_0 = -(\beta F(\beta))|_{\beta=0}, \qquad \bar{\lambda} = \mathrm{d}(\beta F(\beta))/\mathrm{d}\beta|_{\beta=1}, \qquad F(d_0) = 0. \tag{13}$$

The quantities given by (13) are summarized in Table 1 for the parameter values investigated in the paper. Note that the escape rate, the average Lyapunov exponent, and the topological entropy typically have a local maximum in ξ, while the fractal dimension has a tendency to increase with ξ.

[1] In order to better understand Eq. (13), it is worth considering a simple example. Assume that at level n there are b^n ($b > 1$) intervals of equal length $l_i^{(n)} = a^n$ ($a < 1$) in the time delay function. Then $K_0 = \ln b$ and $\kappa = -\ln ab$ immediately follows. The intervals expand in the time reversed dynamics after n steps to a length of order 1, thus $-\ln(l_i^{(n)})/n$ is a kind of local Lyapunov exponent. Since all the intervals have equal length, $\bar{\lambda} = -\ln a$. The intervals of the nth level can be covered by $N(\varepsilon) = b^n$ boxes of size $\varepsilon = a^n$. Thus the fractal dimension is $d_0 = \ln b/\ln(1/a)$. On the other hand, from Eq. (12) $\beta F(\beta) = -\ln b - \beta \ln a$. The validity of the general rules are easy to verify in this simple example. Note, that the graph of $\beta F(\beta)$ is now a straight line corresponding to a behavior governed by one local expansion rate and a monofractal invariant set. In particular, the case of nonchaotic advection due to a single hyperbolic orbit of Lyapunov exponent $\lambda_0 > 0$ is described by a free energy $\beta F(\beta) = \beta\lambda_0$, and hence $K_0 = d_0 = 0$, $\kappa = \bar{\lambda} = \lambda_0$.

Next, we show that the invariant set's dimensions follow from d_0. Using the fact that the dimension of a direct product of two fractals is the sum of the components' fractal dimensions [41], we get that the chaotic saddle's fractal dimension is $d_{\text{set}} = 2d_0$ on the stroboscopic map. The manifolds are the direct product of a line and a Cantor set, therefore, $d_{\text{manifold}} = 1 + d_0$. Thus fractal dimensions of the singularities in the time-delay function uniquely determines the fractality of the chaotic saddle and of its invariant manifolds.

The free energy is, in general, a nonlinear function. In fact, the curvature of $\beta F(\beta)$ contains information concerning multifractal like properties. First, we introduce scaling indices λ by writing

$$\lambda_i = -(1/n)\ln l_i^{(n)} . \tag{14}$$

They tell us how rapidly the length scales decrease with n and can be considered as local *Lyapunov exponents*. The range in which the values λ_i lie is typically a finite interval.

As n grows, there are more and more intervals of the same exponent λ. Their number $W(n,\lambda)$ also grows exponentially, and we can define an entropy function $S(\lambda)$ of the local Lyapunov exponents as the growth rate of W:

$$W(n,\lambda) \sim \mathrm{e}^{S(\lambda)n} , \tag{15}$$

valid for large n. Alternatively, it can be obtained as the Legendre transform of the $\beta F(\beta)$ function: $S(\lambda) = \lambda\beta - \beta F(\beta)|_{\beta=\beta(\lambda)}$, where $\beta(\lambda)$ is defined by $\lambda = d(\beta F(\beta))/\mathrm{d}\beta$. Whenever $F(\beta)$ is not constant, $S(\lambda)$ is a smooth single humped function.

One can define a natural distribution on the chaotic saddle describing how often different pieces of the set are visited by tracer trajectories. For hyperbolic saddles, the measure of a box taken with respect to this natural distribution is proportional to its linear size. More precisely, the measure $P_i^{(n)}$ of each interval covering the saddle along its unstable manifold is proportional to the length of the interval. Normalization implies that

$$P_i^{(n)} \sim \mathrm{e}^{\kappa n} l_i^{(n)} \sim \mathrm{e}^{(\kappa-\lambda_i)n} \tag{16}$$

can be considered as the interval measure. It is then easy to see [39] that the value of λ that belongs to the point where the slope of $S(\lambda)$ is 1 specifies the average Lyapunov exponent $\bar{\lambda}$ of the dynamics. Furthermore, all multifractal spectra, like the $f(\alpha)$ spectrum [42] or the set of generalized entropies K_q [38] can be shown [39] to be expressible by means of $F(\beta)$ or $S(\lambda)$. For the parameter values along the diagonal of Table 1, some of these functions are exhibited in Fig. 13. Notice that in nonchaotic cases the spectra S and f consist of one point only ($S(\lambda_0) = 0, f(0) = 0$); $K_q \equiv 0$, and $F(\beta)$ is a constant (cf. footnote 1). In chaotic cases, the $f(\alpha)$ spectra are shifted with increasing ξ to larger values of α, while their height is increasing. The change of the other characteristic functions is not monotonous with ξ, partially due to the fact that $\bar{\lambda}$ and K_0 have local maxima at $\xi = 5$ and $\xi = 10$, respectively.

We briefly mention that for the parameter values where the chaotic saddle is not fully hyperbolic and the asymptotic behaviour is affected by KAM surfaces, the exponential statistics is no longer valid for very large n. The escape is slower than exponential and can be described by an algebraic decay as $N(n) = n^{-\sigma}$ as $n \to \infty$. This is due to the sticky surface of the KAM tori, where the tracers spend a long time following some approximately quasiperiodic motion. Thus, the escape rate κ is

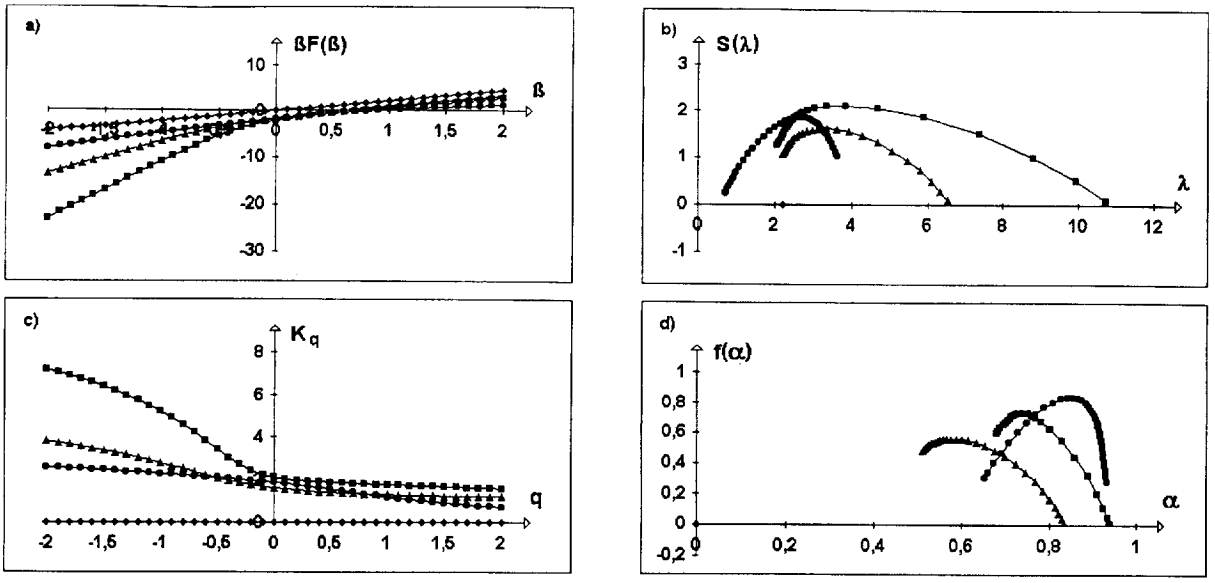

Fig. 13. Geometrical and dynamical multifractal spectra characterizing the tracer dynamics for $\eta = 2$, $\xi = 0.1$ (diamond), $\eta = 1$, $\xi = 5$ (triangle), $\eta = 0.5$, $\xi = 10$ (square), $\eta = 0.1$, $\xi = 20$ (black dot). (a) The free energy functions are determined from time-delay functions like the one in Fig. 12. (b) The spectrum $S(\lambda)$ of the local Lyapunov exponents λ obtained as the Legendre transform of $\beta F(\beta)$. (c) Generalized entropies [38] K_q defined via $\sum_i P_i^{(n)q} \sim \exp((1-q)K_q n)$. They can be expressed with the free energy as $K_q = q(F(q) - \kappa)/(q-1)$. (d) Multifractal spectrum $f(\alpha)$ [42] of the partial dimensions of the nonattracting set. It can be expressed with the entropy function as $f(\alpha) = S(\lambda)/\lambda|_{\lambda = \kappa/(1-\alpha)}$, where α is the crowding index. $f(\alpha)$ is the fractal dimension of intervals of the time delay function with the local scaling property $P_i^{(n)} \sim l_i^{(n)^\gamma}$.

expected to be zero together with the average Lyapunov exponent $\overline{\lambda}$ [43]. The fractal dimension d_0 should converge to $d_0 = 1$ by using very fine resolution [44]. In Table 1 we indicated these asymptotic values where KAM tori are present. In such cases the free energy is identically zero for $\beta \geq 1$ but has a nontrivial branch in the range of $\beta < 1$. These two contributions are associated with the nonhyperbolic and hyperbolic components of the chaotic saddle, respectively. At $\beta = 1$ a "phase transition" occurs. Since such nonanalyticities have been thoroughly investigated in general settings [45], we do not discuss here further details.

Finally, we note that local Lyapunov exponents and other multifractal-like properties can also be determined directly by following the deformation of material lines [46]. Our approach based on the analogy with chaotic scattering provides, however, a simpler method since it requires the analysis of only straight-line segments of an interval, extracted from the time delay function, instead of two-dimensional deformations.

7. Conclusions

The vortex-sink system, or its time reversed version, the vortex-source system, belong to a new class of open flows: they contain singular points with nonzero divergence. As a consequence, fluid

disappears or is created in the course of time. For the advected passive particles this means that the global dynamics is not time reversal invariant. The forward and backward dynamics is different but both are physically realisable. We have shown that the nonattracting invariant set of both dynamics is, however, in common, and of Hamiltonian character.

If the tracer dynamics is chaotic, a strange saddle underlies both the direct and the time reversed dynamics. The invariant manifolds of the saddle play also important roles: the unstable one is traced out by droplets, while the stable one define the fractal basin boundary in both types of dynamics. The structure of dye boundaries in open flows has been the subject of recent papers [28–31, 33]. These boundaries are defined as borderlines between different colours injected into the flow somewhere in the inflow region. It has been shown [29] that in systems where the tracer dynamics is chaotic, the dye boundary has a fractal and a nonfractal part, and the former coincides with one of the invariant manifolds of the chaotic saddle. The question arises, why the basin boundary of our system is entirely fractal and does not contain nonfractal parts. We could, of course, paint the points according to the sink which they exit through or, in the blinking vortex-source problem, according to the place of injection. This type of colouring corresponds to qualitatively different dynamical behaviour (reaching different attractors, or emanating from different repellers). If, however, we subdivide the disk around the vortex centers (the attractor for the repeller of the advection map), say into the upper and lower semidisks, and paint differently with 4 dies, the dye boundary will have also nonfractal components in our system. The preimages (images) of the dividing line segment, however, converge to the saddle's stable (unstable) manifold, and such a manifold will thus be the fractal part of the boundary. Just like in other open flows [33], the fractal dye boundaries will have a surprising topological property, the so-called Wada property [40]. In any neighbourhood of any point on the fractal part of the boundary *particles of all colours used* are present. Thus, not only the chaotic saddle, but also the neighbourhood of its invariant manifolds is *strongly mixing* in such flows.

Acknowledgements

One of us (T.T.) has the privilege to be a colleague of Prof. I. Abonyi, who has continuously shared with him his deep insight into hydrodynamics during the years, this is hereby greatly acknowledged. We thank J. Kadtke, H. Lustfeld, Z. Neufeld, A. Provenzale, and K.G. Szabó for useful discussions. This work was partially supported by the Hungarian Science Foundation under Grant Nos. OTKA T17493, T19483, and the US–Hungarian Science and Technology Joint Funds under Projects 286 and 501.

References

[1] H. Aref, J. Fluid Mech. 143 (1984) 1; D.V. Khakhar, H. Rising, J.M. Ottino, J. Fluid Mech. 172 (1987) 419.
[2] H. Aref, S. Balachandar, Phys. Fluids 29 (1986) 3515.
[3] J. Chaiken, R. Chevray, M. Tabor, Q.M. Tan, Proc. Roy. Soc. London A 408 (1986) 165.
[4] J.M. Ottino, The Kinematics of Mixing: Stretching, Chaos and Transport, Cambridge University Press, Cambridge, 1989; J.M. Ottino, Ann. Rev. Fluid Mech. 22 (1990) 207; S.C. Jana, G. Metcalfe, J.M. Ottino, J. Fluid Mech. 269 (1994) 199.

[5] A. Crisanti, M. Falcioni, G. Paladin, A. Vulpiani, Riv. Nuov. Cim. 14 (1991) 1.
[6] F.J. Muzzio, P.D. Swanson, J.M. Ottino, Int. J. Bifurc. Chaos 2 (1992) 37.
[7] S. Wiggins, Chaotic Transport in Dynamical Systems, Springer, Berlin, 1992.
[8] T.H. Solomon, J.P. Gollub, Phys. Rev. A 38 (1988) 6280; T.H. Solomon, E.R. Weeks, H.L. Swinney, Physica D 76 (1994) 70.
[9] J.C. Sommerer, E. Ott, Science 259 (1993) 281; J.C. Sommerer, Physica D 76 (1994) 85.
[10] D. Elhmaidi, A. Provenzale, A. Babiano, J. Fluid. Mech. 257 (1993) 533; A. Babiano, G. Bofetta, A. Provenzale, A. Vulpiani, Phys. Fluids A 6 (1994) 2465; G. Bofetta, A. Celani, P. Franzese, J. Phys. A 29 (1996) 3749; A. Péntek, J.B. Kadtke, Z. Toroczkai, Phys. Lett. A 224 (1996) 85.
[11] R.T. Pierrehumbert, Chaos Sol. Fract. 4 (1994) 1091.
[12] V.V. Meleshko, G.J.F. van Heijst, Chaos Sol. Fract. 4 (1994) 977.
[13] D. Beigie, A. Leonard, S. Wiggins, Chaos Sol. Fract. 4 (1994) 749.
[14] T. Bohr, J.L. Hansen, Chaos 6 (1996) 554.
[15] K. Shariff, A. Leonard, N.J. Zabusky, J.H. Ferziger, Fluid. Dyn. Res. 3 (1988) 337.
[16] S.W. Jones, H. Aref, Phys. Fluids 31 (1988) 469.
[17] H. Aref, S.W. Jones, S. Mofina, I. Zawadski, Physica D 37 (1989) 423.
[18] S. Jones, O. Thomas, H. Aref, J. Fluid. Mech. 116 (1989) 335; W.R. Young, S. Jones, Phys. Fluids A 3 (1991) 1087.
[19] V. Rom-Kedar, A. Leonard, S. Wiggins, J. Fluid. Mech. 214 (1990) 347.
[20] K. Shariff, T.H. Pulliam, J.M. Ottino, Lect. Appl. Math. 28 (1991) 613.
[21] K. Shariff, A. Leonard, Ann. Rev. Fluid. Mech. 24 (1992) 235.
[22] C. Jung, E. Ziemniak, J. Phys. A 25 (1992) 3929; C. Jung, E. Ziemniak, in: M.M. Novak (Ed.), Fractals in the Natural and Applied Sciences, North-Holland, Amsterdam, 1994; E. Ziemniak, C. Jung, Phys. Lett. A 202 (1995) 263.
[23] C. Jung, T. Tél, E. Ziemniak, Chaos 3 (1993) 555.
[24] E. Ziemniak, C. Jung, T. Tél, Physica D 76 (1994) 123.
[25] J.B. Weiss, Physica D 76 (1994) 230.
[26] G. Károlyi, Diploma work, Eötvös University (in Hungarian) (1995).
[27] G. Stolovitzky, T.J. Kaper, L. Sirovich, Chaos 5 (1995) 671.
[28] Á. Péntek, T. Tél, Z. Toroczkai, J. Phys. A 28 (1995) 2191; Fractals 3 (1995) 33.
[29] Á. Péntek, Z. Toroczkai, T. Tél, C. Grebogi, J.A. Yorke, Phys. Rev. E 51 (1995) 4076.
[30] J. Kennedy, J.A. Yorke, The topology of stirred fluids, preprint, 1995.
[31] M.A. Sanjuan, C. Grebogi, J. Yorke, Chaos 7 (1997) 125; M.A. Sanjuan et al., Phys. Rev. Lett. 78 (1997) 1892.
[32] J.C. Sommerer, H.-C. Ku, H.E. Gilreath, Phys. Rev. Lett. 77 (1996) 5055.
[33] Z. Toroczkai, G. Károlyi, Á. Péntek, T. Tél, C. Grebogi, Y.A. Yorke, Physica A 239 (1997) 235.
[34] U. Smilansky, in: M.J. Giannoni et al., (Eds.), Chaos and Quantum Physics, Elsevier, New York, 1992; C. Jung, Acta Phys. Pol. 23 (1992) 323; E. Ott, T. Tél, Chaos 3 (1993) 417; Z. Kovács, L. Wiesenfeld, Phys. Rev. E 51 (1995) 5476.
[35] N.E. Kochin, I.A. Kibel, N.V. Rose, Theoretical Hydrodynamics, Interscience, New York, 1963.
[36] S. Bleher, C. Grebogi, E. Ott, Phys. Rev. Lett. 63 (1989) 919; Physica D 46 (1990) 87.
[37] T. Tél, in: H. Bai-Lin (Ed.), STATPHYS 19 Directions in Chaos, vol. 3, World Scientific, Singapore, 1990, pp. 149–221.
[38] C. Beck, F. Schlögl, Thermodynamics of Chaotic Systems, Cambridge University Press, Cambridge, 1993.
[39] Z. Kovács, T. Tél, Phys. Rev. Lett. 64 (1990) 1617.
[40] J. Kennedy, J.A. Yorke, Physica D 51 (1991) 213.
[41] K. Falconer, The Geometry of Fractal Sets, Cambridge University Press, Cambridge 1985.
[42] T.C. Halsey, M.H. Jensen, L.P. Kadanoff, I. Procaccia, B.I. Shraiman, Phys. Rev. A 33 (1986) 1141.
[43] F. Christiansen, P. Grassberger, Phys. Lett. A 181 (1993) 47.
[44] Y.T. Lau, J.M. Finn, E. Ott, Phys. Rev. Lett. 66 (1991) 978.
[45] P. Szépfalusy, T. Tél, A. Csordás, Z. Kovács, Phys. Rev. A 36 (1987) 3525; J. Bene, P. Szépfalusy, A. Fülöp, Phys. Rev. A 40 (1989) 4767; M. Feigenbaum, I. Procaccia, T. Tél, Phys. Rev. A 39 (1989) 5359; R. Stoop, J. Parisi, Phys. Rev. A 43 (1991) 1802; G. Radons, Phys. Rev. Lett. 75 (1994) 2518; R. Stoop, Phys. Rev. E 52 (1995)

2216; Z. Kaufmann, H. Lustfeld, J. Bene, Phys. Rev. E 53 (1996) 1416; G. Radons, R. Stoop, J. Stat. Phys. 82 (1996) 1063; R. Stoop, G. Radons, Phys. Rep. 290 (1997) 3, this issue.

[46] A. Vulpiani, Physica D 38 (1989) 372; F. Városi, T.M. Antonsen, Jr., E. Ott, Phys. Fluids A 3 (1991) 1017; D. Beigie, A. Leonard, S. Wiggins, Phys. Rev. Lett. 70 (1993) 275; S. Gallucio, A. Vulpiani, Physica A 212 (1994) 75.